

Towards a predictive scenario of a burning accident in a mining passage

Sinan Demir, Vitaly Bychkov (DECEASED), Sri Hari Ramakrishna Chalagalla & V'yacheslav Akkerman

To cite this article: Sinan Demir, Vitaly Bychkov (DECEASED), Sri Hari Ramakrishna Chalagalla & V'yacheslav Akkerman (2017): Towards a predictive scenario of a burning accident in a mining passage, Combustion Theory and Modelling

To link to this article: <http://dx.doi.org/10.1080/13647830.2017.1328129>



Published online: 31 May 2017.



Submit your article to this journal [↗](#)



View related articles [↗](#)



View Crossmark data [↗](#)



Towards a predictive scenario of a burning accident in a mining passage

Sinan Demir^a, Vitaly Bychkov (DECEASED)^b, Sri Hari Ramakrishna Chalagalla^a and Vyacheslav Akkerman^{a*}

^aCenter for Innovation in Gas Research and Utilization (CIGRU), Center for Alternative Fuels, Engines and Emissions (CAFEE), Department of Mechanical and Aerospace Engineering, West Virginia University, Morgantown, West Virginia 26506-6106, USA; ^bDepartment of Physics, Umea University, Umea 90187, Sweden

(Received 31 October 2016; accepted 27 April 2017)

To reveal the inner mechanisms of a combustion accident in a coalmine, the key stages and characteristics of premixed flame front evolution such as the flame shapes, propagation speeds, acceleration rates, run-up distances and flame-generated velocity profiles are scrutinised. The theories of globally spherical, expanding flames and of finger-flame acceleration are combined into a general analytical formulation. Two-dimensional and cylindrical mining passages are studied, with noticeably stronger acceleration found in the cylindrical geometry. The entire acceleration scenario may promote the total burning rate by up to two orders of magnitude, to a near-sonic value. Starting with gaseous combustion, the analysis is subsequently extended to gaseous-dusty environments. Specifically, combustible dust (e.g. coal), inert dust (e.g. sand), and their combination are considered, and the influence of the size and concentration of the dust particles is quantified. In particular, small particles influence flame propagation more than large ones, and flame acceleration increases with the concentration of a combustible dust, until the concentration attains a certain limit.

Keywords: dust combustion; mining safety; fire safety; Darrieus–Landau instability; finger flame shape

Nomenclature

a_{tip}	flame tip acceleration [m s^{-2}]
B	frequency factor characterising the rate of gas phase oxidation of a gaseous fuel [s^{-1}]
c_s	concentration of coal particles [kg m^{-3}]
c_o	local sound speed [m s^{-1}]
C	constant defined in Equation (2) [m s^{-1}]
C_p	specific heat of gaseous air-fuel mixture [$\text{kJ kg}^{-1} \text{K}^{-1}$]
C_s	specific heat of dust particles [$\text{kJ kg}^{-1} \text{K}^{-1}$]
C_T	entire specific heat [$\text{kJ kg}^{-1} \text{K}^{-1}$]
D_{th}	thermal diffusivity [$\text{m}^2 \text{s}^{-1}$]
E_a	activation energy characterising the gas phase reaction [kJ mol^{-1}]
H	distance to the ignition point from a tunnel side walls [m]

*Corresponding author. Email: Vyacheslav.Akkerman@mail.wvu.edu

Δh_{CH_4}	specific enthalpy of formation for methane [kJ kg ⁻¹]
k	perturbation wave-number [m ⁻¹]
k_{DL}	Darrius–Landau (DL) cut-off wave number [m ⁻¹]
k_u	thermal conductivity [W K ⁻¹ m ⁻¹]
Le	Lewis number
L_f	flame thickness [m]
L_v	heat necessary for gasification per unit volume [kJ m ⁻³]
m_{fuel}	total amount of fuel available per unit volume (accounting for the volatilities) [kg m ⁻³]
m_{CH_4}	mass of methane available for combustion per unit volume [kg m ⁻³]
m_{air}	mass of air available for combustion per unit volume [kg m ⁻³]
M_{CH_4}	molar mass of methane [kg mol ⁻¹]
M_{air}	molar mass of air [kg mol ⁻¹]
n_s	number of particles per unit volume [m ⁻³]
n_{air}	number of moles of air per unit volume [mol]
n	exponent given in Equation (1)
N	exponent given in Equation (40)
P	pressure [Pa]
Pr	Prandtl number
R	characteristic length scale [m]
R_f	radius of the flame skirt [m]
R_u	universal gas constant [kJ mol ⁻¹ K ⁻¹]
r	radial (cylindrical) coordinate [m]
r_s	radius of a single particle [μ m]
S_L	unstretched laminar flame propagation velocity in gaseous environment [m s ⁻¹]
$S_{L,d}$	unstretched laminar flame propagation velocity in gaseous-dusty environment [m s ⁻¹]
T	temperature [K]
T_b	adiabatic flame temperature [K]
T_f	flame temperature with particles [K]
T_s	surface temperature of a dust particle [K]
T_u	temperature of the reactants [K]
T_v	devolatilisation temperature [K]
t	time [s]
t_r	residence time [s]
t_{sph}	characteristic time when the spherical flame transforms into a finger-shaped front [s]
t_{wall}	time when the flame skirt contacts a wall [s]
u	velocity [m s ⁻¹]
U_{DL}	instantaneous global flame speed with respect to the fuel mixture [m s ⁻¹]
U_{tip}	flame tip velocity [m s ⁻¹]
V_s	volume of a single particle [m ³]
x	radial (2D) coordinate [m]
Ze	Zeldovich number
Z_{rud}	run-up-distance [m]
Z_{tip}	flame tip position [m]
z	axial coordinate [m]
Q	heat released during combustion per unit volume [kJ m ⁻³]

- w'_v devolatilisation rate [$\text{kg m}^{-3} \text{s}^{-1}$]
 w_v total mass of volatilities released per unit volume [kg m^{-3}]

Greek symbols

- Θ thermal expansion coefficient
 ϕ gaseous mixture equivalence ratio
 ϕ_s modified equivalence ratio due to the addition of coal particles
 σ_{DL} growth rate of the Darrieus–Landau (DL) instability [s^{-1}]
 ρ density of a coal-dust/gas mixture [kg m^{-3}]
 ρ_s density of a dust single particle [kg m^{-3}]
 ρ_u density of a gas mixture [kg m^{-3}]
 Γ coefficient defined in Equation (3)
 λ_{DL} DL cut-off wavelength [m]

Subscripts

- s coal dust particle
 u ambient conditions
 1 air-fuel mixture
 2 burnt matter

1. Introduction

Historically, the mining industry has one of the highest injury and fatality rates for employees. While mining accidents are caused by a multitude of reasons, spontaneous methane deflagrations and detonations in the presence of coal dust constitute the most common hazard. Among the recent examples of such dust/gas disasters, the 2014 mining catastrophe in Soma, Turkey resulted in over 300 deaths. To reduce the risk of these accidental burning events, researchers worldwide analyse – experimentally, theoretically and computationally – numerous factors affecting the mechanisms of flame propagation and acceleration in methane–air and methane–air–coal-dust mixtures. In particular, Chatrathi et al. [1] investigated methane–air flame propagation in industrial-scale piping. Silvestrini et al. [2] provided simplified formulas to evaluate the flame velocities as well as the run-up distances of the deflagration-to-detonation transition (DDT) for flammable mixtures in smooth and obstructed tubes. Chen et al. [3] studied the structure and dynamics of flames at various equivalence ratios; they suggested that flame acceleration occurs only after a transition to turbulence, which actually determines the structure of the flame front. In another study, Bi et al. [4] investigated premixed methane–air flames in relatively long pipes by means of numerical simulations. Kjaldman [5] performed a pioneering numerical study on burning in a gaseous environment with combustible dust impurities, employing a computational fluid dynamics (CFD) tool with small-scale dust flames. Furthermore, Liu et al. [6] conducted experiments on coal-dust–air mixture explosions under a weak ignition condition in a horizontal tube of diameter ~ 0.2 m. Skjold et al. [7] investigated, experimentally and numerically, constant-volume dusty/gaseous detonations. Houim et al. [8] simulated the interaction of shock waves and the resulting shear layers with coal-dust layers. Gardner et al. [9] undertook large-scale experiments to investigate detonations spreading in flowing coal-dust–air suspensions in a duct of diameter 0.6 m. Bartknecht [10,11] performed experiments on coal-dust–air detonations in two tubes of different diameters and lengths; the maximum flame speeds attained in a tube of length 130 m and diameter 2.5 m were 500 m s^{-1} and 700 m s^{-1} , for dust concentrations of 250 g m^{-3} and 500 g m^{-3} , respectively.

Nevertheless, up to now there was not a unified analysis capturing all the fundamentals and providing enough details about a flame acceleration mechanism, starting from the initial stages of the process to the onset of the detonation. The present work is a step in this direction. Earlier experiments by Oppenheim [12] and Urtiew [13] were devoted to hydrogen-oxygen flame acceleration, at the initial stage of burning, and transition to detonation. It was concluded that an initially laminar accelerating flame creates compression and then shock waves ahead of it, which subsequently leads to flame turbulisation and the detonation onset. Clanet and Searby [14] have identified a finger-shaped mechanism of flame acceleration at the early stages of burning in tubes, which has been subsequently justified numerically and developed into a quantitative theory [15]. Specifically, a flame propagating in a cylindrical tube with ideally slip adiabatic walls was considered, with one end of the tube closed, and a flame ignited at the symmetry axis at the closed end, and propagating to the open one. In that case, the flame front develops from a hemispherical shape at the beginning to a finger-shape, accompanied by the concomitant exponential growth of the surface area of the flame front and, thereby, associated increase in the flame velocity. This acceleration is fast, but it lasts only for a short time interval – until a flame skirt contacts a wall. This acceleration mechanism is Reynolds-independent, and is therefore equally strong in micro-tubes and mining passages. However, in practice, Re-dependent factors such as combustion instabilities and/or turbulence provide corrections to the flame acceleration scenario, making it Reynolds-dependent as well [16].

Similar to any premixed flame, one of the key flame characteristics in the present study is the unstretched laminar flame velocity, S_L , which is a function of thermal-chemical properties of the fuel mixture; in particular, the fuel-to-oxidiser equivalence ratio ϕ . For methane–coal-dust flames, the laminar flame velocity also depends on the coal-dust parameters such as the size and concentration of the coal-dust particles. At the same time, realistically, a flame front is not planar, but strongly corrugated; thereby, the flame consumes more fuel per unit time and propagates faster. Table 1 summarises the typical factors causing flame corrugation/acceleration. In this work, we employ some of them to quantify the mining flame scenario and fix a relevance of any particular mechanism to the mining passage geometry.

First, an initially smooth flame front is subjected to the cellular (Darrieus–Landau, DL) instability [17]. While this effect is negligible in micro/meso-scales, it gets stronger with an increase in size, providing a 2.5–10 increase in the flame velocity in tunnels of a human height size (1.7–2 m diameter) [18,19]. Second, when a flame front starts to approach the tunnel side wall, it acquires a finger-like shape [14,15,20]. Then the flame surface area grows quite fast, promoting the flame velocity by one more order of magnitude by the time when the flame skirt contacts the wall [15]. Thereafter, this acceleration stops. In

Table 1. Various mechanisms of flame corrugation/acceleration in tunnels/channels.

Factors causing flame corrugation/acceleration	Re-dependence	Relevance to mines	Relevance to micro-scales
Flame instability	Yes, \uparrow Re	Yes	No
Finger flame	No	Yes	Yes
Wall friction	Yes, \downarrow Re	Yes	Yes
Obstacles	No	Yes	Yes
Turbulence	Yes	Yes	Yes

the present work, we combine the first mechanism with the second one, for the first time, in order to predict and quantify the timing and locus of these stages in a coalmine. As a result, within the laminar approach, we provide a quantitative predictive scenario of a premixed methane–air burning accident in a mining passage – from the earlier stage of flame acceleration until the transition to a detonation.

Among other potential factors that may influence the process, we mention the effects of wall friction [21] and obstacles [22], as well as post-finger tulip flame formation and turbulence [23], leading to a flame-shock interaction until a detonation onset [24]. In future studies, the role of turbulence may potentially be incorporated into the present formulation, as an option, by replacing the laminar flame velocity S_L by a local turbulent flame velocity S_T , with the ratio S_T/S_L obtained analytically, or computationally from a relevant turbulent flame speed model, or phenomenologically from an experiment. As for flame acceleration due to wall friction [25], it weakens significantly with the Reynolds number, thereby being minor in a coalmine. In contrast, a “tooth-brush” array of in-built obstacles generates extremely fast flame acceleration, and this mechanism is Re-independent as well, which makes it potentially relevant to the mining geometry if obstacles are large enough [22]. However, the role of obstacles in mining accidents requires a separate investigation, which will be undertaken elsewhere.

Overall, in the present work, we are developing a predictive and quantitative scenario of a mining accident, aiming to provide guidance for preventing and mitigating disasters associated with gaseous deflagrations and detonations in coalmines. The analytical formulation is presented in Section 2, while Section 3 is devoted to the parametric study. Specifically, we identify the key characteristics for different stages of the process and predict the timing and the burning rate for each stage. It is shown that the combustion instabilities and finger flame acceleration may promote flame propagation velocity by up to two orders of magnitude and even trigger detonation (which constitutes a conceptual disaster in mines, because of shocks, even beyond its combustion nature). The input parameters for the formulation include the equivalence ratio, the transport properties of the air–methane–coal-dust mixture, as well as the size and concentration of the coal-dust particles (with the laminar flame velocity and the thermal expansion coefficient coupled to them). Another set of parameters is coupled to the size and configuration of a mining passage.

2. Analytical formulation

In the present work, we employ a low Mach-number model [15], which is relatively simple and provides reasonable evaluations even in the case of compressible flows; see a justification in [20] for more details (a rigorous extension of this formulation accounting for the compressibility effects will be presented elsewhere). Specifically, here we consider an accidental ignition of a methane–air (or propane–air) mixture that occurred at a distance H from a tunnel sidewall, as illustrated in Figure 1(a). An embryonic flame propagates outwardly from the ignition point. It is initially spherically smooth as any tendency to excite a combustion instability is suppressed by the stretch-effect induced by an expanding flame. The process is controlled by the interplay between the flame stretch and the mixture (non)equi-diffusion. The critical issue at an early stage of burning is whether an embryonic flame can sustain. In this respect, the flame front evolution depends on the Lewis number Le (the thermal-to-mass diffusivities ratio) such that sustained combustion is possible for $Le > 1$ mixtures, whereas for $Le < 1$ ones, a flame embryo needs to attain a minimum radius, through the initial spark energy, before sustained propagation is possible [26,27].

Consequently, keeping $Le < 1$ in a mining environment may improve the flame safety standards. It is also noted that $Le \sim 1$ for the majority of methane–air flames.

Stage 1: Quasi-spherical, self-similar accelerative flame expansion

Let us consider the case when a flame has survived and keeps propagating. In the present study, we are interested mostly in large scales such that the flame stretch will eventually be neglected. At the early stage of burning, the flame front expands with a constant speed, $dR_f/dt = \Theta S_L$, with respect to the ignition point, where $R_f(t)$ is the instantaneous flame radius, S_L the unstretched laminar flame propagation speed, as discussed above, and $\Theta = \rho_u/\rho_b$ is the thermal expansion factor, which is coupled to the equivalence ratio ϕ . As a flame “ball” grows in size and the stretch intensity reduces, the diffusional-thermal cells would develop over the surface of $Le < 1$ flames [28]. Subsequently, the flame thickness relative to the global flame radius is reduced, leading to the onset of hydrodynamic (DL) flame instability mode. The latter generates hydrodynamic cells over the flame surface, regardless of Le , and will eventually dominate in the surface morphology [28,29]. The continuous generation of new cells leads to the continuous increase in the flame surface density and thereby an expanding flame self-accelerates in a scale-invariant (self-similar) manner; see Figure 1(b). According to numerous experimental and computational studies, a reasonable fitting law for such acceleration is [30]:

$$R_f = R_0 + Ct^n \approx Ct^n, \quad (1)$$

where R_0 plays the role of a critical radius related to the transition to the cellular flame structure (it can be neglected within the frame of a large-scale formulation), $n \approx 1.3 - 1.4$ in the most of studies; and the factor C can be evaluated as [30,31]:

$$C = k_{DL}^{n-1} (\Theta S_L/n)^n, \quad (2)$$

where k_{DL} is the DL cut-off wavenumber that appears in the Pelce–Clavin dispersion relation [32]:

$$\sigma_{DL}(k) = \Gamma(\Theta) S_L k (1 - k/k_{DL}), \quad \Gamma(\Theta) = \frac{\Theta}{\Theta + 1} \left[\left(\Theta + 1 - \frac{1}{\Theta} \right)^{1/2} - 1 \right], \quad (3)$$

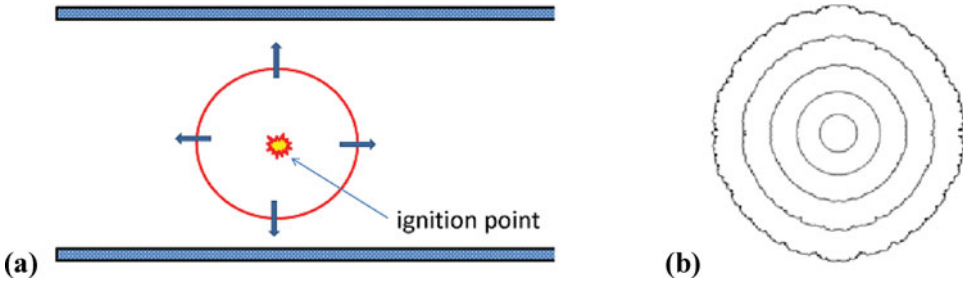


Figure 1. Illustration of quasi-spherical flame expansion: the stages of ignition, uniform propagation of a smooth front (a) as well as self-similar acceleration of a cellular front (b).

and it is coupled to the DL critical wavelength as $k_{DL} = 2\pi/\lambda_{DL}$; the latter, in turn, depends on Θ and is proportional to the flame thickness, which is conventionally defined as $L_f = D_{th}/S_L$, where D_{th} is the thermal diffusivity, with $\lambda_{DL} \approx (30 - 100)L_f$ for $\Theta = 5 - 8$. In the present work, we employ the following formulas for λ_{DL} and, respectively, k_{DL} [23]:

$$\lambda_{DL} = 2\pi L_f \left(1 + \frac{(\Theta + 1)}{(\Theta - 1)^2} \Theta \ln \Theta \right), \quad k_{DL} = L_f^{-1} \left(1 + \frac{(\Theta + 1)}{(\Theta - 1)^2} \Theta \ln \Theta \right)^{-1}. \quad (4)$$

With power-law flame acceleration, Equation (1), the global (radial) flame velocity with respect to the ignition point is not a constant ΘS_L any more, but a time-dependent quantity:

$$dR_f/dt = nCt^{n-1} = (k_{DL}/n)^{n-1} (\Theta S_L)^n t^{n-1}. \quad (5)$$

To evaluate the instantaneous global flame velocity with respect to the fuel mixture, we divide the result (5) by Θ , namely:

$$U_{DL} = \frac{1}{\Theta} \frac{dR_f}{dt} = \frac{nC}{\Theta} t^{n-1} = S_L^n \left(\frac{\Theta}{n} k_{DL} \right)^{n-1} t^{n-1}. \quad (6)$$

Stage 2: Finger-like flame acceleration

Generally speaking Equations (1)–(6) describe the accelerative flame expansion in an opening. In practice, as soon as a flame front approaches (even before contacting) the tunnel/channel wall, the difference between the radial and the axial flow velocities modifies the flame shape, forming two outwardly propagating finger-like fronts, as illustrated in Figure 2. In fact, the expansion of the burning matter leads to a strong flow in the axial direction, which drifts the tip of a finger-shaped flame. Due to the elongated shape, the surface area of such a flame front is much larger than the passage cross section, which causes the flame to accelerate. However, this acceleration stops when a flame “skirt” contacts a passage wall. By the end of this process, the distance from the ignition point to the flame tip is much larger than the passage radius.

We next combine the analysis of an expanding flame with a finger-flame formulation [15] such that a time-dependent quantity U_{DL} , Equation (6), is incorporated instead of the

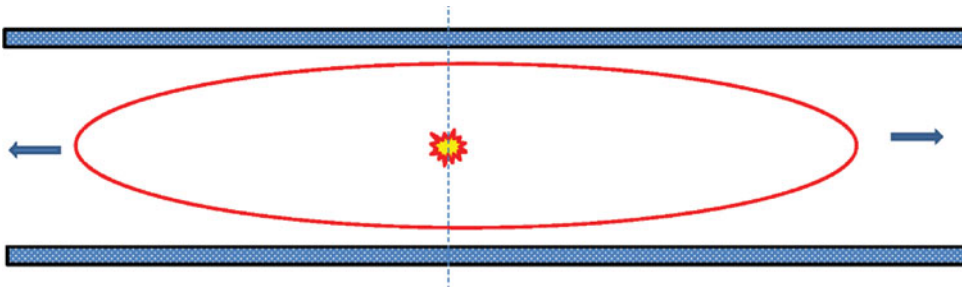


Figure 2. Illustration of finger-like flame acceleration.

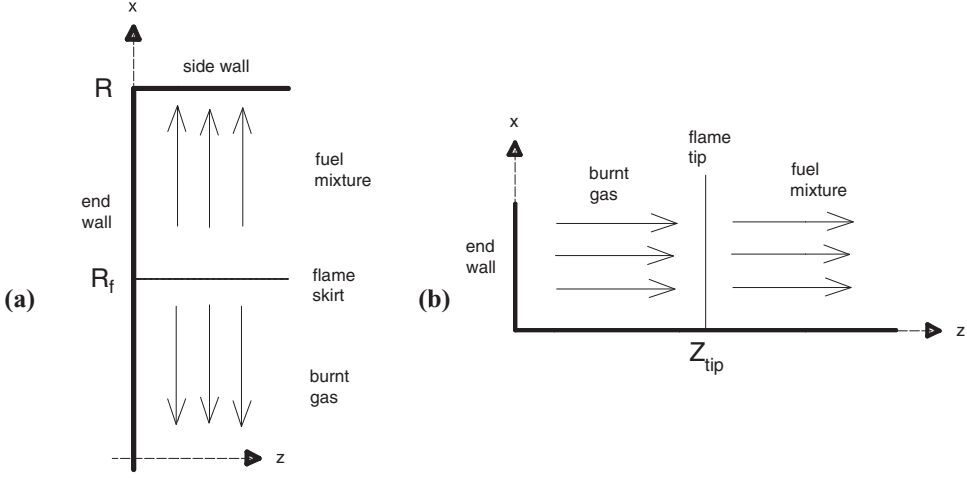


Figure 3. Flow close to tunnel end wall (a) and axis (b).

constant S_L . The rationale for such a consideration is the scale- and time-separations between the formulations: the tunnel width is much larger than the DL cells, and the finger-flame acceleration is much stronger than that associated with the DL instability. To generalise the approach, both the two-dimensional (2D) planar and cylindrical geometries are considered and compared. In fact, a real coalmine tunnel may have a rectangular/square cross section, which is actually neither 2D nor cylindrical, but in between. In the following subsections, Section 2.1 and Section 2.2, we develop the analytical formulations for 2D-planar and cylindrical-axisymmetric geometries, respectively.

2.1. 2D planar geometry

The sketch of the coordinate system for the flow near the end-wall and the centreline of the tunnel is shown in Figure 3. We start with a 2D geometry. Then the incompressible continuity equation reads:

$$\frac{\partial u_x}{\partial x} + \frac{\partial u_z}{\partial z} = 0. \quad (7)$$

The boundary conditions are $u_z|_{z=0} = 0$, $u_x|_{x=R_f} = 0$. By assuming a potential flow, the axial and radial flow velocities ahead of (subscript 1) and behind (subscript 2) the flame front read:

$$u_{z,1} = A_1(t)z, \quad u_{x,1} = A_1(t)(H - x), \quad u_{z,2} = A_2(t)z, \quad u_{x,2} = -A_2(t)x, \quad (8)$$

where the factors A_1 and A_2 depend on time only. While the flow is generally rotational in the burnt matter (with singularity occurring), due to a curved shape of the flame front, the flow can be treated as potential close to the end-wall, where a flame front is locally planar. The matching conditions at a flame front, $x = R_f$, are:

$$\frac{dR_f}{dt} - u_{x,1} = U_{DL}(t), \quad u_{x,1} - u_{x,2} = (\Theta - 1)U_{DL}(t), \quad u_{z,1} = u_{z,2}, \quad (9)$$

where the first equation specifies the flame propagation velocity with respect to the fuel mixture, the second describes the jump of the normal velocity, and the third describes the continuity of the tangential velocity. Substituting Equation (8) into Equation (9), we obtain $A_1(t) = A_2(t) = (\Theta - 1)U_{DL}(t)/H$, and then the evolution equation for the flame skirt reads:

$$\frac{dR_f}{dt} = \left\{ (\Theta - 1) \left(1 - \frac{R_f}{H} \right) + 1 \right\} U_{DL} = \left\{ (\Theta - 1) \left(1 - \frac{R_f}{H} \right) + 1 \right\} S_L^n \left(\frac{\Theta}{n} k_{DL} \right)^{n-1} t^{n-1}, \quad (10)$$

with the initial condition $R_f|_{t=0} = 0$, and the solution:

$$\begin{aligned} t(R_f) &= \left\{ \frac{\Theta H}{(\Theta - 1)C} \ln \left(\frac{\Theta H}{\Theta H - (\Theta - 1)R_f} \right) \right\}^{1/n} \\ &= \frac{n}{\Theta S_L} \left\{ \frac{\Theta H}{(\Theta - 1)k_{DL}^{n-1}} \ln \left(\frac{\Theta H}{\Theta H - (\Theta - 1)R_f} \right) \right\}^{1/n}, \end{aligned} \quad (11)$$

$$\begin{aligned} \frac{R_f(t)}{H} &= \frac{\Theta}{\Theta - 1} \left\{ 1 - \exp \left[-\frac{\Theta - 1}{\Theta H} C t^n \right] \right\} \\ &= \frac{\Theta}{\Theta - 1} \left\{ 1 - \exp \left[-\frac{\Theta - 1}{\Theta H} \left(k_{DL}^{n-1} \left(\frac{\Theta S_L}{n} \right)^n \right) t^n \right] \right\}. \end{aligned} \quad (12)$$

The characteristic time instant devoted to the transition from a globally-spherical to a finger-like flame shape, t_{sph} , and the associated flame skirt location, $R_f(t_{sph})$, can be evaluated as:

$$\begin{aligned} t_{sph} &\approx \left(\frac{\Theta H}{(\Theta - 1)C} \right)^{1/n} = \frac{n}{\Theta S_L} \left(\frac{\Theta H}{(\Theta - 1)k_{DL}^{n-1}} \right)^{1/n}, \\ R_f(t_{sph}) &= \frac{(1 - e^{-1})\Theta H}{(\Theta - 1)} \approx 0.632 \frac{\Theta H}{(\Theta - 1)}, \end{aligned} \quad (13)$$

with the burning rate at this instant being:

$$U_{DL}(t_{sph}) = \frac{nC}{\Theta} t_{sph}^{n-1} = n \left(\frac{C}{\Theta} \right)^{1/n} \left(\frac{H}{\Theta - 1} \right)^{\frac{n-1}{n}}. \quad (14)$$

We next focus on the flame tip, which evolution equation reads:

$$\frac{dZ_{tip}}{dt} = (\Theta - 1)U_{DL}(t) \frac{Z_{tip}}{H} + \Theta U_{DL}(t), \quad (15)$$

with the initial condition $Z_{tip}|_{t=0} = 0$, and the solution:

$$\begin{aligned} Z_{tip} &= \frac{\Theta H}{(\Theta - 1)} \left\{ \exp \left[\frac{(\Theta - 1)C}{\Theta} \frac{t^n}{H} \right] - 1 \right\} \\ &= \frac{\Theta H}{(\Theta - 1)} \left\{ \exp \left[\frac{(\Theta - 1)k_{DL}^{n-1}}{\Theta} \frac{(\Theta S_L)^n}{H} t^n \right] - 1 \right\}. \end{aligned} \quad (16)$$

The flame skirt (in fact, its first “wing”) contacts the tunnel side wall when $R_f = H$, i.e.:

$$t_{wall,1} = \left\{ \frac{\Theta H}{(\Theta - 1)C} \ln(\Theta) \right\}^{1/n} = \frac{n}{\Theta S_L} \left\{ \frac{\Theta H}{(\Theta - 1)k_{DL}^{n-1}} \ln(\Theta) \right\}^{1/n}. \quad (17)$$

The second flame wing contacts the opposite wall a little later, when $R_f = 2R - H$:

$$t_{wall,2} = \left\{ \frac{\Theta(2R - H)}{(\Theta - 1)C} \ln(\Theta) \right\}^{1/n} = \frac{n}{\Theta S_L} \left\{ \frac{\Theta(2R - H)}{(\Theta - 1)k_{DL}^{n-1}} \ln(\Theta) \right\}^{1/n}. \quad (18)$$

Obviously, $t_{wall,1} = t_{wall,2}$ if $H = R$ and $t_{wall}/t_{sph} = \sqrt[n]{\ln \Theta}$. The velocity of the flame tip in the laboratory reference frame and its acceleration are respectively given by:

$$\frac{dZ_{tip}}{dt} = U_{tip} = nCt^{n-1} \exp\left(\frac{(\Theta - 1)Ct^n}{\Theta H}\right), \quad (19)$$

$$\frac{d^2Z_{tip}}{dt^2} = a_{tip} = nCt^{n-1} \exp\left(\frac{(\Theta - 1)Ct^n}{\Theta H}\right) \left\{ (n - 1)t^{-1} + nt^{n-1} \frac{\Theta - 1}{\Theta} \frac{C}{H} \right\}. \quad (20)$$

One can also readily check that in the case of $n = 1$, the DL instability disappears and all these formulas reproduce their counterparts of [20].

2.2. Cylindrical axisymmetric geometry

We next develop a similar analytical formulation for the cylindrical-axisymmetric geometry. In this case, the continuity equation for the incompressible flow reads [15]

$$\frac{1}{r} \frac{\partial (ru_r)}{\partial r} + \frac{\partial u_z}{\partial z} = 0, \quad (21)$$

with the boundary conditions $u_z|_{z=0} = 0$, $u_r|_{r=R_f} = 0$. Similar to the 2D case, assuming potential flow in the fuel mixture, we find

$$u_{z,1} = A_1(t)z, \quad u_{r,1} = \frac{A_1(t)}{2} \left(\frac{H^2}{r} - r \right), \quad u_{z,2} = A_2(t)z, \quad u_{r,2} = -\frac{A_2(t)}{2}r. \quad (22)$$

The matching conditions are given by Equation (9). Then $A_1(t) = A_2(t) = 2(\Theta - 1)U_{DL}(t)R_f/H^2$. Altogether, Equations (6) and (21)–(22) provide the evolution equation for the flame skirt:

$$\frac{dR_f}{dt} = \left\{ \Theta - (\Theta - 1) \frac{R_f^2}{H^2} \right\} U_{DL} = \left\{ \Theta - (\Theta - 1) \frac{R_f^2}{H^2} \right\} S_L^n \left(\frac{\Theta}{n} k_{DL} \right)^{n-1} t^{n-1}, \quad (23)$$

with the solution:

$$t(R_f) = \left\{ \frac{\Theta H}{2\alpha C} \ln \left(\frac{\Theta + \alpha(R_f/H)}{\Theta - \alpha(R_f/H)} \right) \right\}^{1/n} = \frac{n}{\Theta S_L} \left\{ \frac{\Theta H}{2\alpha k_{DL}^{n-1}} \ln \left(\frac{\Theta + \alpha(R_f/H)}{\Theta - \alpha(R_f/H)} \right) \right\}^{1/n}, \quad (24)$$

$$\frac{R_f(t)}{H} = \frac{\Theta}{\alpha} \tanh \left(\frac{\alpha C t^n}{\Theta H} \right) = \frac{\Theta}{\alpha} \tanh \left(\frac{\alpha}{\Theta H} k_{DL}^{n-1} \left(\frac{\Theta S_L}{n} \right)^n t^n \right), \quad (25)$$

where $\alpha = \sqrt{\Theta(\Theta - 1)}$. The characteristic time instant devoted to the transition from a globally spherical to a finger-like flame shape, t_{sph} , and the flame skirt location at this instant, $R_f(t_{sph})$, can be evaluated as:

$$t_{sph} \approx \left(\frac{\Theta H}{2\alpha C} \right)^{1/n} = \frac{n}{\Theta S_L} \left(\frac{\Theta H}{2\alpha k_{DL}^{n-1}} \right)^{1/n}, \quad R_f(t_{sph}) = \frac{\Theta H}{\alpha} \tanh(0.5) \approx 0.46 \sqrt{\frac{\Theta}{\Theta - 1}} H, \quad (26)$$

with the associated corrugated flame velocity being:

$$U_{DL}(t_{sph}) = \frac{nC}{\Theta} t_{sph}^{n-1} = n \left(\frac{C}{\Theta} \right)^{1/n} \left(\frac{H}{2\alpha} \right)^{(n-1)/n}. \quad (27)$$

We next focus on the flame tip, which evolution equation in this geometry reads:

$$\frac{dZ_{tip}}{dt} = 2(\Theta - 1)U_{DL}(t) \frac{R_f(t)Z_{tip}}{H^2} + \Theta U_{DL}(t), \quad (28)$$

with the solution:

$$Z_{tip} = \frac{\Theta H}{2\alpha} \sinh \left(2 \frac{\alpha C t^n}{\Theta H} \right) = \frac{H}{2} \sqrt{\frac{\Theta}{\Theta - 1}} \sinh \left(2 \sqrt{\frac{\Theta - 1}{\Theta}} \frac{k_{DL}^{n-1}}{H} \left(\frac{\Theta S_L}{n} \right)^n t^n \right). \quad (29)$$

The first wing of the flame skirt contacts the tunnel side wall when $R_f = H$, i.e.:

$$t_{wall,1} = \left\{ \frac{\Theta H}{2\alpha C} \ln \left(\frac{\Theta + \alpha}{\Theta - \alpha} \right) \right\}^{1/n} = \frac{n}{\Theta S_L} \left\{ \frac{\Theta H}{2\alpha k_{DL}^{n-1}} \ln \left(\frac{\Theta + \alpha}{\Theta - \alpha} \right) \right\}^{1/n}. \quad (30)$$

The second flame wing contacts the opposite wall at:

$$t_{wall,2} = \left\{ \frac{\Theta(2R - H)}{2\alpha C} \ln \left(\frac{\Theta + \alpha}{\Theta - \alpha} \right) \right\}^{1/n} = \frac{n}{\Theta S_L} \left\{ \frac{\Theta(2R - H)}{2\alpha k_{DL}^{n-1}} \ln \left(\frac{\Theta + \alpha}{\Theta - \alpha} \right) \right\}^{1/n}, \quad (31)$$

when $R_f = 2R - H$. Obviously, $t_{wall,1} = t_{wall,2}$ if $H = R$ and $t_{wall}/t_{sph} = \sqrt[n]{\ln[(\Theta + \alpha)/(\Theta - \alpha)]}$. The flame tip velocity and acceleration in the laboratory reference frame read:

$$\frac{dZ_{tip}}{dt} = U_{tip} = nCt^{n-1} \cosh\left(\frac{2\alpha Ct^n}{\Theta H}\right), \quad (32)$$

$$\frac{d^2z_{tip}}{dt^2} = a_{tip} = nCt^{n-2} \left\{ \frac{2\alpha nCt^n}{\Theta H} \sinh\left(\frac{2\alpha nCt^n}{\Theta H}\right) + (n-1) \cosh\left(\frac{2\alpha nCt^n}{\Theta H}\right) \right\}. \quad (33)$$

Again, in the case of $n = 1$, the DL instability disappears and all these formulas reproduce their counterparts of [20].

3. Results and discussion

In this section, the analytical results of Section 2 are thoroughly investigated for a set of input parameters. Specifically, we start with the gaseous methane–air or propane–air flames, of various equivalence ratios, and then extend the analysis to methane–air–coal–dust combustion.

3.1. Homogeneously gaseous flames

While it is a methane–air accidental explosion that is most relevant to coalmines, for comparison, and to identify the role of the type of a combustible, here we also investigated potential propane–air flame spreading. The thermal expansion factor Θ and the laminar flame velocity S_L are tabulated versus the equivalence ratio ϕ : in Table 2, for the methane–air mixture, and in Table 3, for the propane–air one, respectively [33]. Based on these tables, the characteristic timings of the process, t_{sph} , Equations (13) and (26), and t_{wall} , Equations (17), (18) and (30), (31) are presented in Figures 4 and 5 for the 2D planar and cylindrical axisymmetric geometries, respectively, with $n = 1.4$ and $R = H = 1.05$ in both figures. It is recalled that these quantities, t_{sph} and t_{wall} , play the key roles for flame acceleration and, thereby, the entire flame evolution scenario. Indeed, just after an ignition, a flame tip moves in the same manner as the flame skirt, Equations (10)–(12) and (23)–(25), exhibiting a globally spherical (cellular) shape of an expanding flame front while $t < t_{sph}$. Then the flame skirt slows down, while the flame tip accelerates, thereby leading to very strong elongation and global acceleration of the flame front within the interval $t_{sph} < t < t_{wall}$. This acceleration is nevertheless limited in time: it terminates as soon as the flame skirt contacts a wall, $t = t_{wall}$. The flame tip position, velocity and acceleration are presented in Figures 6–8 for the planar and cylindrical geometries. Here, Figures 6(a), 7(a) and 8(a) show the time evolution of these quantities, in a stoichiometric

Table 2. Methane–air flame parameters [33].

ϕ	0.6	0.7	0.8	0.9	1	1.1	1.2	1.3	1.4
Θ	5.54	6.11	6.65	7.12	7.48	7.55	7.43	7.28	7.09
S_L (m s ⁻¹)	0.089	0.169	0.254	0.325	0.371	0.383	0.345	0.250	0.137

Table 3. Propane–air flame parameters [33].

ϕ	0.63	0.7	0.8	0.9	1	1.1	1.2	1.3	1.4
Θ	6.04	6.56	7.15	7.66	8.02	8.08	8	7.88	7.74
S_L (m s ⁻¹)	0.147	0.217	0.303	0.374	0.418	0.429	0.399	0.322	0.226

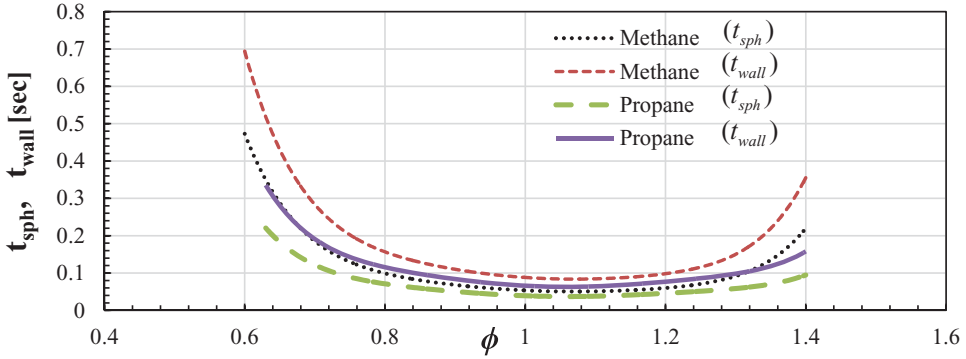


Figure 4. 2D planar geometry: The time limitations of the finger flame acceleration, t_{sph} (Equation (13)) and t_{wall} (Equation (17)), versus the equivalence ratio ϕ for propane–air and methane–air flames, $R = H = 1.05$ m, $n = 1.4$.

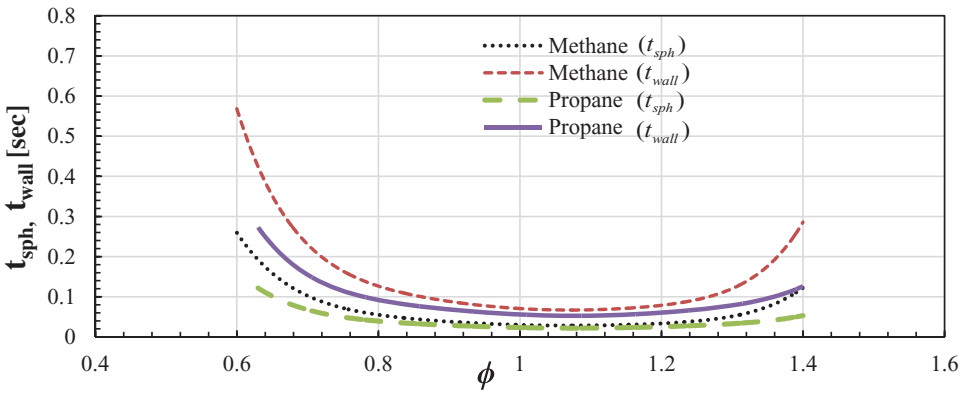


Figure 5. Cylindrical axisymmetric geometry: The time limitations of the finger flame acceleration, t_{sph} (Equation (26)), and t_{wall} (Equation (30)), versus the equivalence ratio ϕ for propane–air and methane–air flames, $R = H = 1.05$ m, $n = 1.4$.

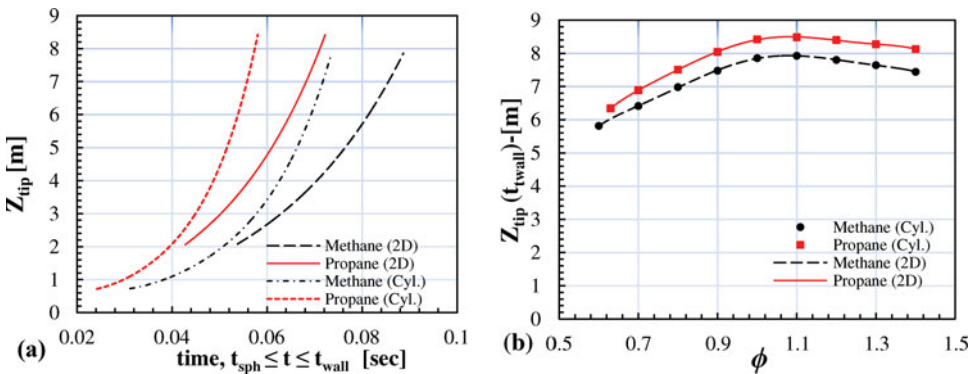


Figure 6. (a) Evolution of flame tip position Z_{tip} in a stoichiometric ($\phi = 1$) mixture and (b) $Z_{tip}(t_{wall})$ versus ϕ for methane–air and propane–air combustion in the 2D planar and cylindrical axisymmetric geometries.

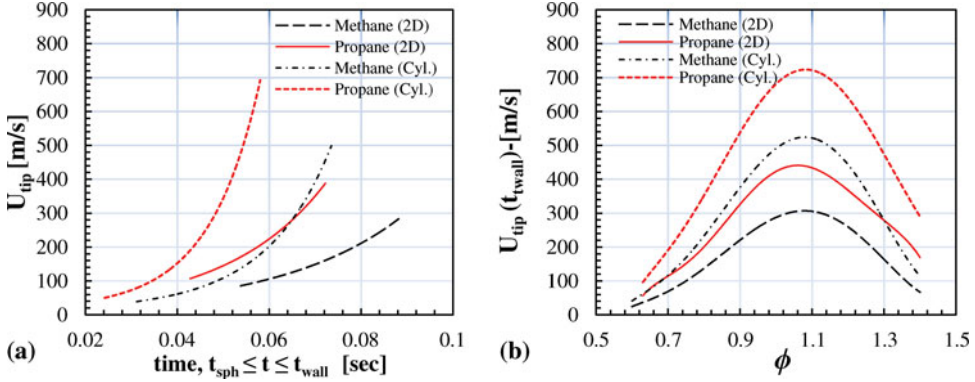


Figure 7. (a) Evolution of flame tip velocity U_{tip} in a stoichiometric ($\phi = 1$) mixture and (b) $U_{tip}(t_{wall})$ versus ϕ for methane–air and propane–air combustion in the 2D-planar and cylindrical-axisymmetric geometries.

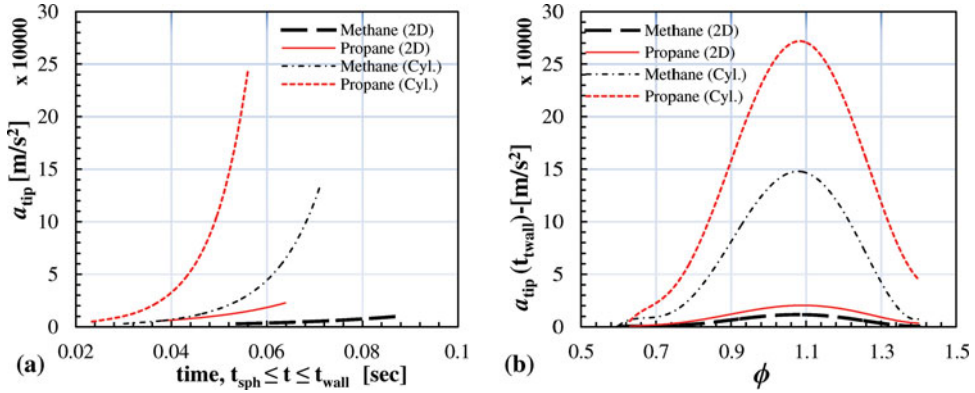


Figure 8. (a) Evolution of flame tip acceleration a_{tip} in a stoichiometric ($\phi = 1$) mixture and (b) $a_{tip}(t_{wall})$ versus ϕ for methane–air and propane–air combustion in the 2D-planar and cylindrical-axisymmetric geometries.

mixture, $\phi = 1$, while Figures 6(b), 7(b) and 8(b) present the maximal quantities, attained during finger flame acceleration, versus the equivalence ratio ϕ , namely: $Z_{tip} \equiv Z_{tip}(t_{wall}) \equiv \Theta H$, Equations (16) and (29); $\dot{Z}_{tip} \equiv U_{tip}(t_{wall})$, Equations (19) and (32); and $\ddot{Z}_{tip} \equiv a_{tip}(t_{wall})$, Equations (20) and (33), respectively. It is seen that a propane–air flame generally spans a greater distance before it contacts a wall, which can be attributed to its higher laminar flame velocity S_L at a given equivalence ratio. Besides, a higher flame tip velocity and, thereby, stronger acceleration are attained in the cylindrical configuration as compared to the 2D geometry.

As a result, the impacts of globally spherical and finger-like flame acceleration mechanisms are both significant in a mining passage, and they may trigger detonation more effectively in a cylindrical configuration than in a 2D one. Specifically, in both geometries, the whole process takes less than 0.1 s, during which a flame tip travels around 8 m (Figure 6). The tip of a methane flame front attains the velocities of 300 m s^{-1} and 500 m s^{-1} (in the laboratory reference frame) in the 2D planar and cylindrical cases, respectively (Figure 7(a)), thus exceeding the nominal value S_L by three orders of magnitude,

and the laminar flame velocity in the laboratory reference frame, ΘS_L , by two orders. For propane–air combustion, the burning rate increases even higher, up to 400 m s^{-1} and 700 m s^{-1} in the 2D planar and cylindrical axisymmetric geometries, respectively. In fact, it is [Figure 7](#) that identifies whether a propagating flame front can attain a sonic/supersonic speed in a coalmine, where a detonation occurs mostly due to an accidental ignition of methane, being thereby one of the major causes for a disaster. For methane–air burning, while such an overcome of the sound barrier is not observed in a 2D channel, in a cylindrical geometry, it occurs for the equivalence ratios in the range $0.9 \leq \phi \leq 1.2$. For faster propane–air burning, this range is even wider in the cylindrical geometry, $0.8 \leq \phi \leq 1.3$, and it is also observed in a 2D planar geometry for $1.0 \leq \phi \leq 1.2$. Consequently, we may expect a deflagration-to-detonation transition (DDT) event to occur in all these cases.

In fact, a reasonable and conventional parameter to analyse flame acceleration as a stage of the DDT process is the so-called *run-up distance*. Two distinctive definitions for such a quantity are frequently employed in the DDT studies: (i) a distance that a flame span from its ignition to the detonation onset; or (ii) a distance at which the flame velocity in the laboratory reference frame equals the sound speed. In the first case, the run-up distance strongly depends on particular chemical kinetics of the reactions involved. In contrast, in the latter case, the run-up distance is a purely gas-dynamic characteristic of the process. Since we are focusing on the gas-dynamics of flame acceleration, the second definition is employed in this paper, namely the run-up distance is approximated as the flame tip position at the instant when its velocity equals the local sound speed, $dZ_{tip}/dt = U_{tip} = c_o$. Although it is recognised that such a definition is not accurate, and the detonation does not occur exactly at that instant, still these values correlate, and therefore this is a reasonable approximation. Similarly, we may also define the *run-up time* as the instant when the flame speed in the laboratory reference frame overcomes the sound barrier. For the 2D planar geometry, the run-up timing, t_{rud} , can be obtained by equating [Equation \(19\)](#) to the sound speed:

$$c_o = \left. \frac{dZ_{tip}}{dt} \right|_{r.u.d} = U_{tip}|_{r.u.d} = nCt_{rud}^{n-1} \exp\left(\frac{(\Theta - 1)Ct_{rud}^n}{\Theta H}\right), \quad (34)$$

and then, substituting this result into [Equation \(16\)](#), we find the run-up distance in the form

$$Z_{rud} = \frac{\Theta H}{\Theta - 1} \left\{ \exp\left[\frac{(\Theta - 1)Ct_{rud}^n}{\Theta H}\right] - 1 \right\}. \quad (35)$$

The cylindrical counterparts of these quantities are obtained in the same manner by using [Equations \(32\)](#) and [\(29\)](#), which yield:

$$c_o = \left. \frac{dZ_{tip}}{dt} \right|_{r.u.d} = U_{tip}|_{r.u.d} = nCt_{rud}^{n-1} \cosh\left(\frac{2\alpha Ct_{rud}^n}{\Theta H}\right), \quad (36)$$

$$Z_{rud} = \frac{\Theta H}{2\alpha} \sinh\left(\frac{2\alpha Ct_{rud}^n}{\Theta H}\right). \quad (37)$$

All these results are shown in [Figure 9](#), which identifies the distance the flame propagates before the detonation onset.

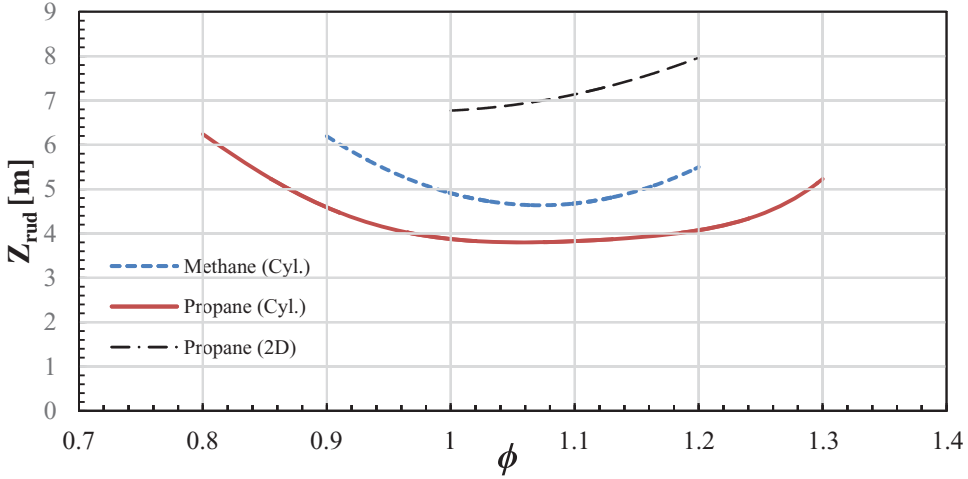


Figure 9. The run-up distance, Z_{rud} , versus the equivalence ratio ϕ for methane–air flames, in a cylindrical geometry, and for propane–air flames, in both 2D-planar and cylindrical geometries.

3.2. Extension to gaseous-dusty environment

We next extend our formulation from combustion of a purely gaseous methane–air mixture to that with coal-dust impurities. For this purpose, we implement the Seshadri formulation [34] that expresses the “gaseous-dusty” unstretched laminar flame velocity, $S_{d,L}$, as a function of local thermal-chemical properties of the gas and coal dust in the form:

$$S_{d,L} = \frac{1}{Ze} \sqrt{\frac{2Bk_u}{\rho_u C_T} \exp\left(-\frac{E_a}{R_u T_f}\right)}, \quad Ze = \frac{E_a (T_f - T_u)}{R_u T_f^2}, \quad (38)$$

where E_a is the activation energy, Ze the Zel’dovich number, and:

$$C_T = C_p + C_s n_s \frac{4\pi r_s^3 \rho_s}{3 \rho} \quad (39)$$

the whole specific heat of the mixture, with C_p and C_s being that of the gas and coal dust particles, respectively. Here ρ is the density of the mixture, which can be expressed as $\rho = \rho_u + c_s$, where ρ_u is the fresh gas density and c_s the concentration of particles. The quantity $n_s = (c_s/\rho_s)/V_s$ is the number of particles per unit volume, with $V_s = 4\pi r_s^3/3$ being the volume of a single particle and r_s being the radius of this particle. The laminar flame velocity, $S_{d,L}$, can generally increase or decrease in the presence of coal particles. On the one hand, the flame speed is promoted by the effect of volatiles released from the coal particles through the gaseous mixture, which is accounted as an additional fuel source for the combustion process in the reaction zone. As a result, the growth of the equivalence ratio promotes the flame temperature and, thereby, the flame propagation velocity. On the other hand, the coal dust particles gain heat from the flame during the devolatilisation process, thereby acting as a heat sink. This reduces the flame temperature and, thereby, the flame velocity [35]. To be specific, [34] suggested the following expression for the devolatilisation rate of the coal particles (the mass of a gaseous fuel vaporised per unit

volume per second):

$$w'_v = An_s 4\pi r^2 T_s^N. \quad (40)$$

In this study, we use $A = 3.4 \cdot 10^{-5} \text{kg m}^{-2} \text{s}^{-1} \text{K}^{-1}$, $N = 1.33$ as in [34]. The temperature of a coal particle is approximated as $T_s = (T_v + T_b)/2$, where T_v is the devolatilisation temperature, which is taken here to be 600 K, and T_b is the adiabatic flame temperature based on the purely methane–air equivalence ratio. Among various methods to find T_b , here it is evaluated as a fifth-order polynomial function of the equivalence ratio [36]:

$$T_b = (-2.21 \times 10^4)\phi^5 + (8.042 \times 10^4)\phi^4 + (-1.171 \times 10^5)\phi^3 + (8.471 \times 10^4)\phi^2 + (-2.854 \times 10^4)\phi + 4.89 \times 10^3, \quad (41)$$

valid in the range $0.6 \leq \phi \leq 1.6$. The characteristic time of vaporisation is of the order of [34]:

$$t_r = \frac{k_u}{\rho_u S_L^2 C_T}, \quad (42)$$

which is the residence time of a coal particle before it enters the reaction zone. It is noted that S_L in Equation (42) is actually the laminar propagation velocity of a gaseous flame (without particles) for a given equivalence ratio, and this quantity can be calculated by removing the coal dust particles in Equation (39), i.e. by substituting $C_T = C_p$ in Equation (38). In our case, to match the calculated laminar flame velocity in the case of no particles, we simply take the experimental values of S_L given in Table 2. The characteristic time of vaporisation, t_r , is used to estimate the total mass of released volatiles per unit volume, $w_v = w'_v t_r$. Similar to [34], for simplicity, this additional fuel is assumed to be methane (CH_4), which is added to the original gaseous methane–air mixture, thereby promoting the equivalence ratio. The new amount of gaseous fuel per unit volume in the mixture is designated as $m_{fuel}^m = m_{CH_4}^m + w_v$, where $m_{CH_4}^m$ is the original mass of methane per unit volume for a given equivalence ratio, and it can be calculated together with that for air as:

$$m_{CH_4}^m = \frac{M_{CH_4} V_{CH_4} P}{R_u T_u (V_{CH_4} + V_{air})}, \quad m_{air}^m = \frac{M_{air} V_{air} P}{R_u T_u (V_{CH_4} + V_{air})}. \quad (43)$$

Here P is the atmospheric pressure, V_{CH_4} and V_{air} , M_{CH_4} and M_{air} are the volumes and molar masses of methane and air, respectively. Accordingly, the modified equivalence ratio can be estimated as:

$$\phi_s = \frac{\left[(m_{fuel}^m / M_{CH_4}) / (m_{air}^m / M_{air}) \right]_{act}}{\left[(m_{CH_4}^m / M_{CH_4}) / (m_{air}^m / M_{air}) \right]_{st}}. \quad (44)$$

With this modified equivalence ratio, a new flame temperature, T_f^* , is estimated by Equation (41). The outcome for a methane–air premixed flame is shown in Figure 13(a), where T_f^* is presented versus the coal dust concentration c_s for various equivalence ratios, $\phi = 0.7; 0.8; 0.9; 1$. To match the experimental values of Table 2 in the case of no

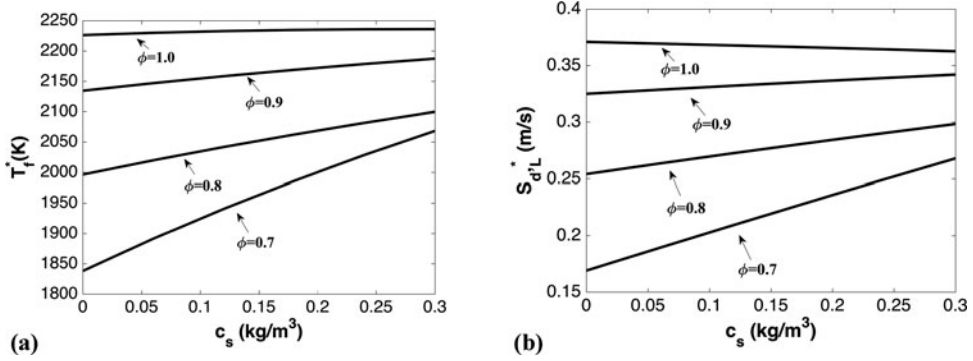


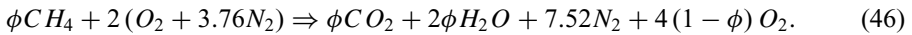
Figure 10. The flame temperature T_f^* (a) and laminar velocity $S_{d,L}^*$ (b) modified by the promotion of the equivalence ratio, versus the particle concentration c_s for the particles of size $r_s = 25 \mu\text{m}$.

coal-dust particles, we modify Equation (38) as:

$$S_{d,L} = S_L \sqrt{\frac{\phi_s}{\phi}} \sqrt{\frac{C_P}{C_T} \left(\frac{T_f}{T_b}\right)^2} \left(\frac{T_b - T_u}{T_f - T_u}\right) \sqrt{\frac{E(T_f - T_b)}{T_f T_b R_u}}. \quad (45)$$

The corresponding values of T_f^* are then used to estimate the new laminar flame velocity, $S_{d,L}^*$, by substituting T_f^* instead of T_f into Equation (45). The results are shown in Figure 10 for particles of radius $r_s = 25 \mu\text{m}$. Table 4 [37] presents other values used in the present analysis. It is seen that both T_f^* and $S_{d,L}^*$ grow with the increase in c_s and/or ϕ . It is also noted that while the new flame temperature and laminar flame velocity grow significantly with c_s for lean combustion, $\phi = 0.7$, these c_s -dependences weaken with the increase in ϕ such that T_f^* and $S_{d,L}^*$ appear almost c_s -invariant for $\phi = 1$. This is due to an effective promotion of the equivalence ratio at $\phi = 0.7$ resulting from the increase in the flame temperature T_f^* .

Unlike a combustible (e.g. coal) particle, an inert (e.g. sand) particle acts only as a heat sink, because it absorbs heat from the flame and reduces the flame temperature. For lean ($\phi < 1$) or stoichiometric ($\phi = 1$) methane–air combustion, the global chemical reaction reads:



The heat release in the process of burning of ϕ moles of methane and 9.52 moles of air equals $[(T_b - T_u) \sum C_P \cdot n_{product}]$. With the assumption that the entire heat released in the reaction is used to raise the temperature of the mixture, the volumetric heat release from

Table 4. Some physical parameters used in the study [37].

B (s^{-1})	3.5×10^6	ρ_u (kg m^{-3})	1.135
k_u ($\text{W K}^{-1} \text{m}^{-1}$)	0.052	ρ_s (kg m^{-3})	1000
E (kJ mol^{-1})	88.8	C_p ($\text{kJ kg}^{-1} \text{K}^{-1}$)	2.22
R_u ($\text{kJ mol}^{-1} \text{K}$)	8.314×10^{-3}	C_s ($\text{kJ kg}^{-1} \text{K}^{-1}$)	1.26

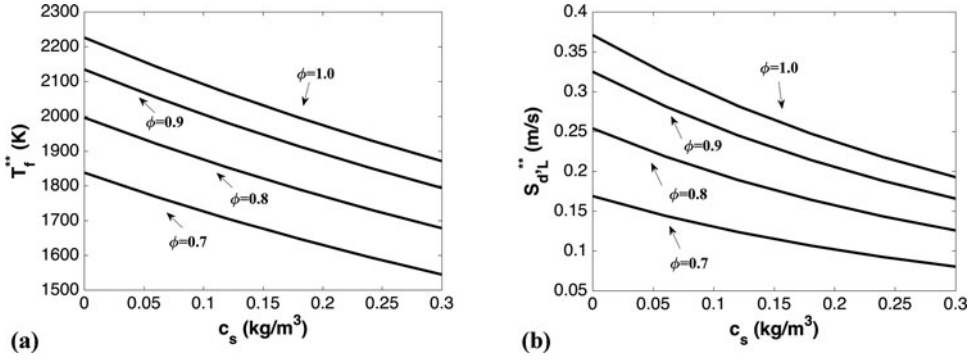


Figure 11. The flame temperature T_f^{**} (a) and laminar velocity $S_{d,L}^{**}$ (b), modified by the heat sink effect, versus the particle concentration c_s for the particles of size $r_s = 25 \mu\text{m}$.

methane–air combustion of a given equivalence ratio can be found as:

$$Q = \left[(T_b - T_u) \sum C_P \cdot n_{product} \right] \frac{n_{air}}{9.52 (V_{CH_4} + V_{air})}, \quad (47)$$

where $n_{product}$ is the number of moles of the burning products, which depends on ϕ . Assuming that a flame with particles releases the same amount of heat while it is also influenced by the temperature rise of particles, a secondly revised flame temperature, T_f^{**} , can be estimated using the energy conservation law:

$$Q = \left[(T_f^{**} - T_u) \sum C_P \cdot n_{product} \right] \frac{n_{air}}{9.52 (V_{CH_4} + V_{air})} + c_s C_s (T_f^{**} + T_u) + L_v. \quad (48)$$

Rearranging Equation (48), we finally express this revised flame temperature as:

$$T_f^{**} = \frac{Q - L_v}{\frac{n_{air}}{9.52 (V_{CH_4} + V_{air})} \sum C_P n_{product} + c_s C_s} + T_u, \quad (49)$$

where L_v is the heat of gasification per unit volume, which is given by $L_v = 0.01 w_v \Delta h_{CH_4}$ [37].

Equation (49) for the revised flame temperature, which accounts for the heat sink effect, indicates a continuous decrease in the flame temperature with the addition of the inert particles. It is subsequently used to estimate the revised laminar flame velocity, $S_{d,L}^{**}$, by substituting T_f^{**} instead of T_f into Equation (45). The results are presented in Figure 11, where the revised flame temperature and laminar flame velocity are shown versus the dust concentration c_s for various equivalence ratios, $\phi = 0.7; 0.8; 0.9; 1$. It is seen that both T_f^{**} and $S_{d,L}^{**}$ decrease with c_s , and such a decrease get promoted with ϕ . At the same time, T_f^{**} and $S_{d,L}^{**}$ grow with ϕ . This effect becomes more profound with the increase in ϕ .

Finally, a combined effect of the increase in the equivalence ratio and that of the heat sink can be accounted by averaging the flame temperature over those associated with both effects separately, $T_f^{***} = (T_f^* + T_f^{**})/2$ [37]. It is noted, in this respect, that such a definition of T_f^{***} is solely based on the work by Xie et al. [37], while an alternative definition would influence the subsequent results quantitatively. In fact, an accurate knowledge of the flame

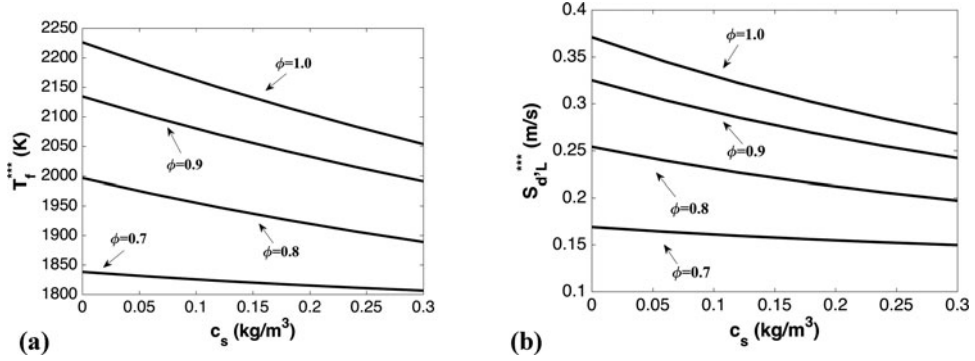


Figure 12. The flame temperature T_f^{***} (a) and laminar velocity $S_{d,L}^{***}$ (b), modified to the combined (combustible + inert) effect, versus the particle concentration c_s for the particles of size $r_s = 25 \mu\text{m}$.

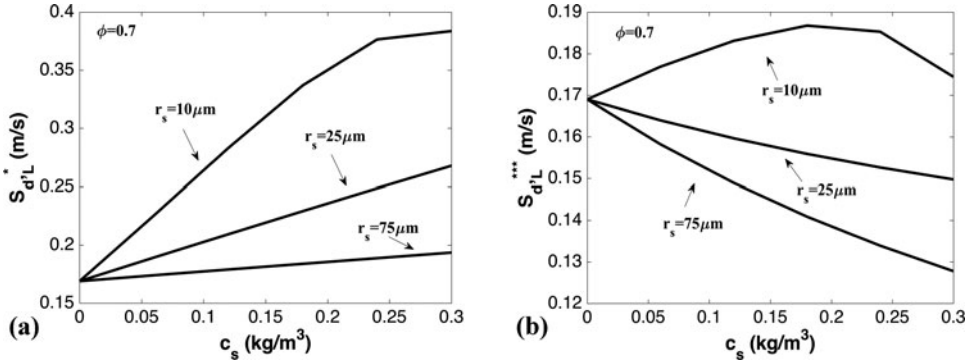


Figure 13. The modified flame velocity versus the particle concentration for the fixed equivalence ratio ($\phi = 0.7$) and various particle radii ($r_s = 10, 25$ and $75 \mu\text{m}$) for combustible (a) and combined (combustible + inert) (b) particles.

temperature is clearly crucial in predicting the flame velocity accurately, in particular, due to the exponential dependence in Equation (38). Again, the new laminar flame velocity $S_{d,L}^{***}$ is calculated by substituting T_f^{***} instead of T_f into Equation (45). Figure 12 is a counterpart of Figure 11 for T_f^{***} and $S_{d,L}^{***}$ instead of T_f^{**} and $S_{d,L}^{**}$, respectively. Similar to Figure 11, the increase in ϕ promotes both T_f^{***} and $S_{d,L}^{***}$. However, the dependence on the dust concentration changes: namely, while the c_s -dependences of T_f^{***} and $S_{d,L}^{***}$ resemble that of T_f^{**} and $S_{d,L}^{**}$ for stoichiometric combustion, Figure 11, these near-linear dependences weaken with the decrease in ϕ such that the effects of the promoted equivalence ratio and heat sink are practically balanced for $\phi = 0.7$, making thereby T_f^{***} and $S_{d,L}^{***}$ almost c_s -invariant. This result is opposite to that observed in Figure 10 for T_f^* and $S_{d,L}^*$. Besides, in the case of no particles ($c_s = 0$), all our results for the flame velocity reproduce the experimental data of Table 2.

The effect of a particle radius on the laminar flame velocity in the case of both combustible and combined (combustible + inert) particles is shown in Figure 13, for the fixed equivalence ratio $\phi = 0.7$ and various particle radii $r_s = 10; 25; 75 \mu\text{m}$, consistent with the realistic coal particle sizes, in both cases. In the case of combustible particles, the laminar flame velocity attains its highest value for $r_s = 10 \mu\text{m}$. This can be devoted to the effect of faster pyrolysis in small coal particles, which causes effective increase in the equivalence

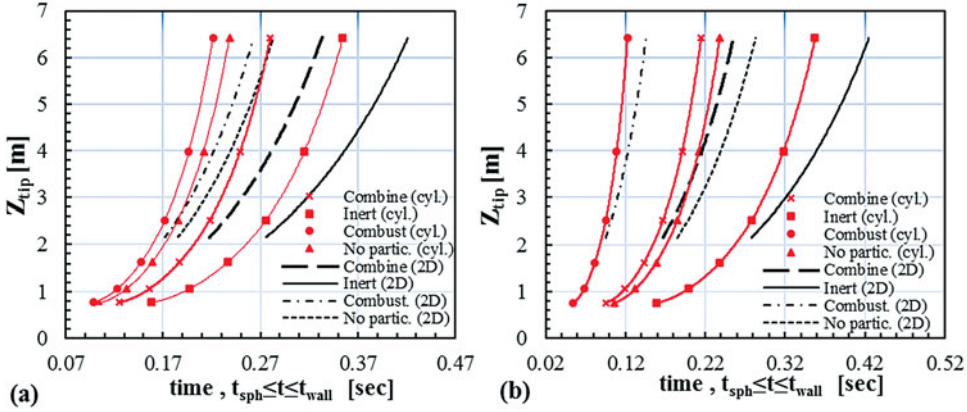


Figure 14. Evolution of flame tip position Z_{tip} in a homogeneous gaseous environment and in the presence of combustible, inert, and combined particles in both 2D and cylindrical geometries for $\phi = 0.7$, $c_s = 120 \text{ g cm}^{-3}$ and $r_s = 75 \text{ }\mu\text{m}$ (a), $r_s = 10 \text{ }\mu\text{m}$ (b).

ratio, see Equation (44). However, the growth of $S_{d,L}^*$ moderates around $c_s = 180 \text{ g cm}^{-3}$ and becomes almost constant close to value of $c_s = 250 \text{ g cm}^{-3}$. This decreasing trend in the slope of $S_{d,L}^*$ is mainly caused by an effective increase in the equivalence ratio from $\phi = 0.7$ at $c_s = 0$ till $\phi = 1.05$ at $c_s = 300 \text{ g cm}^{-3}$. Such a strong increase in ϕ shows a decreasing slope in the laminar flame velocity when it approaches the stoichiometric value. This observation can also be justified by remembering how the adiabatic flame temperature changes with the equivalence ratio. On the other hand, small particles, $r_s = 10 \text{ }\mu\text{m}$, promote the laminar flame velocity $S_{d,L}^{***}$ as long as the concentration does not exceed $c_s = 180 \text{ g cm}^{-3}$, i.e. as long as the heat sink effect plays a minor role. However, with the increase in the particle concentration, the heat sink effect becomes dominant and causes a decreasing trend in $S_{d,L}^{***}$. Besides, relatively larger particles, with $r_s = 25 \text{ }\mu\text{m}$ and $r_s = 75 \text{ }\mu\text{m}$, monotonically reduce the flame velocity with the increase in the particle concentration.

We next incorporate these updates on the laminar flame velocity into the formulation of Section 2 on gaseous combustion, thereby modifying the results of Section 3.1. Specifically, we update the scenarios of globally spherical flame expansion and that of finger flame acceleration accounting for the presence of combustible and/or inert particles, both for planar and cylindrical geometries. As we incorporate the modified equivalence ratios and the modified laminar flame velocities into the formulations of Section 2, all the functions of the equivalence ratio and laminar flame velocity will change accordingly, and they also modify the timing and key characteristics of the flame dynamics such as the evolution of the flame tip position and velocity. Figures 14 and 15 compare the situations of combustible, inert and both types of particles as well as that with no particles. Specifically, Figure 14(a) presents the evolution of the flame tip for methane–air–dust burning of equivalence ratio $\phi = 0.7$ and particle concentration $c_s = 120 \text{ g cm}^{-3}$ for the 2D planar and cylindrical axisymmetric geometries. The particles of two different sizes, $r_s = 75 \text{ }\mu\text{m}$ and $r_s = 10 \text{ }\mu\text{m}$, are employed in Figure 14(a) and 14(b), respectively. Figure 15(a) and 15(b) are respectively the counterparts of Figure 14(a) and 14(b) for the flame tip velocity. Figures 14 and 15 justify the expectation that flame propagation is facilitated by combustible dust but it is mitigated by inert dust. It is also noted that small particles, $r_s = 10 \text{ }\mu\text{m}$, Figures 14(b) and 15(b), both combustible and combustible + inert, impact flame propagation noticeably

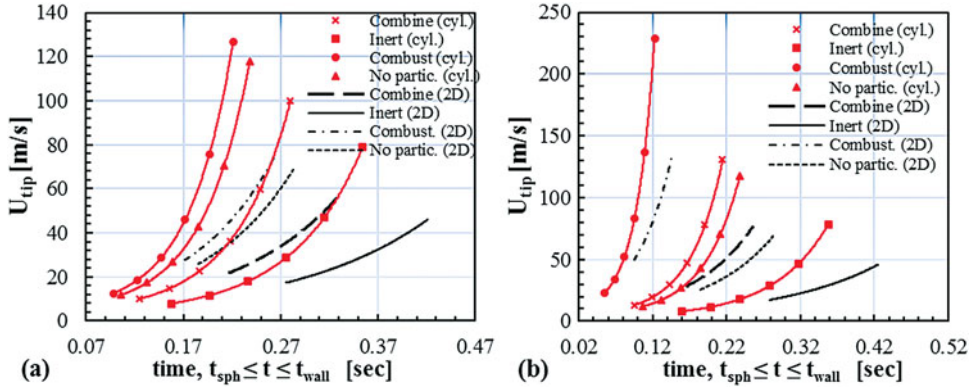


Figure 15. Evolution of flame tip position U_{tip} in a homogeneous gaseous environment and in the presence of combustible, inert, and combined particles in both 2D and cylindrical geometries for $\phi = 0.7$, $c_s = 120 \text{ g m}^{-3}$ and $r_s = 75 \mu\text{m}$ (a), $r_s = 10 \mu\text{m}$ (b).

stronger than that of $r_s = 75 \mu\text{m}$, Figures 14(a) and 15(a). In particular, while the difference between the cases of no particles and combustible particles is hardly seen for $r_s = 75 \mu\text{m}$ in the cylindrical geometry, such a difference is substantial for $r_s = 10 \mu\text{m}$, both in the 2D planar and cylindrical axisymmetric configurations. The difference between the cases of no particles and that of combined particles becomes relatively small in the cylindrical geometry. Additionally, in line with Section 3.1, the flame tip velocity attains higher values for all (combustible, inert, combined combustible + inert and no particles) cases in the cylindrical geometry as compared to a 2D one, hence yielding faster flame propagation. Such a qualitative and quantitative difference is demonstrated in Figures 14 and 15.

We have also investigated the effect of particles concentration on the instantaneous flame tip velocity $U_{tip}(t_{sph}, t_{wall})$ for the combustible, inert and combined combustible + inert dust for the equivalence ratio $\phi = 0.7$ and the particle radius $r_s = 25 \mu\text{m}$. The result is shown in Figure 16, for the 2D (a) and cylindrical (b) geometries. Specifically, the flame tip velocities attained at the time instants t_{sph} and t_{wall} increase with the concentration of the combustible dust as long as the $c_s < 250 \text{ g cm}^{-3}$. In contrast, the flame tip velocity diminishes with the concentration of the inert dust. For a given particle size and equivalence ratio, the increase or decrease in the combined particles concentration does not influence $U_{tip}(t_{sph})$. For the same particle type, $U_{tip}(t_{wall})$ slightly increases with the concentration while $c_s < 200 \text{ g cm}^{-3}$ but then decreases when $c_s > 200 \text{ g cm}^{-3}$.

Finally, it is noted that different motions of dust particles may influence the fire evolution. Moreover, distribution of the particle velocities will lead to a non-uniform distribution of the dust concentration and thereby a certain spatial distribution of the local burning properties such as that of equivalence ratio ϕ_s , laminar flame velocity $S_{d,L}$, etc. In fact, the coal dust distribution is typically non-uniform in coalmines and a stationary dense coal dust layer may spread through the bottom of the channel. In particular, a gaseous-based detonation wave may produce a strong shock that can lift and entrain the dust layer. Over time, the shock weakens but the shock-heated fluid is ignited by lifted dust, which initiates a secondary combustion process [38]. Such a lifted dust layer may resemble a linear, cubic, or even parabolic distribution of the dust concentration in space, due to the different energy levels of complex magnetic forces.

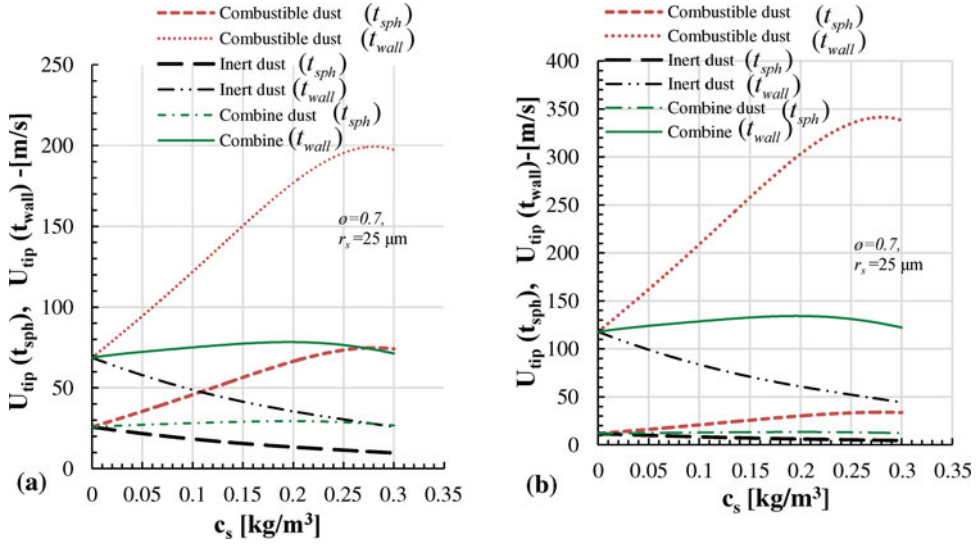


Figure 16. Instantaneous flame tip velocities $U_{tip}(t_{sph})$ and $U_{tip}(t_{wall})$ versus the particle concentration c_s for combustible, inert and combined particles for $\phi = 0.7$ and $r_s = 25 \mu\text{m}$ in the 2D-planar (a) and cylindrical-axisymmetric (b) geometries.

The impact of these local spatial variations of the burning properties on the global flame propagation scenario requires a separate study that will be presented elsewhere [39]. Specifically, this question is addressed in [39] by incorporating the spatial functions, such as the linear, cubic and parabolic distributions mentioned above instead of a constant n_s , in the analysis.

4. Conclusion

In the present paper, we undertook a step towards developing a predictive quantitative scenario of burning accidents in coalmines. For this purpose, in Section 2, the analysis of globally spherical expanding corrugated flames [30] was combined with the finger flame formulation [14,15,20]. The study considered both the 2D planar (Section 2.1) and the cylindrical axisymmetric (Section 2.2) geometries. A higher flame tip velocity and, thereby, stronger acceleration were attained in the cylindrical geometry as compared to a 2D-planar one. While it is methane that typically explodes in coalmines, propane burning is also considered herein, for comparison. We started with purely gaseous combustion (Section 3.1), and then extended the analysis to the coal-dust-gas environments by means of the Seshadri formulation [34] for the unstretched laminar flame velocity. In this respect, combustible (e.g. coal) and inert (e.g. sand) dust particles of various concentrations (0–300 g m⁻³) and sizes (10–75 μm), as well as their combination, are investigated. It is noted that small particles of radius $r_s = 10 \mu\text{m}$, combustible or inert, influence flame propagation noticeably more than larger particles of radius $r_s = 75 \mu\text{m}$. The instantaneous flame tip velocity grows with the concentration of the combustible dust as long as the concentration does not exceed 250 g cm⁻³. In contrast, the flame velocity monotonically decreases with the concentration of inert dust. In particular, for a given particle size $r_s = 25 \mu\text{m}$ and equivalence ratio $\phi = 0.7$, the increase or decrease in the concentration does not impact

the flame velocity due to a balance between the effects of the equivalence ratio and the heat sink.

We have predicted and quantified the key stages and characteristics of coalmine burning such as the evolution and velocity of the tip and skirt of the flame front as well as the locus and timing of a potential detonation onset. The timing for each stage as well as the flame shapes, propagation speeds, acceleration rates, run-up distances and flame-generated velocity profiles were identified. Specifically, when an accidental ignition occurs in a coalmine, first, an embryonic flame develops from a smooth hemispherical/hemi-circular kernel to a globally spherical/cellular (corrugated) structure. This occurs due to the Darrieus–Landau flame instability, and the process is accompanied by self-similar flame acceleration. Subsequently, such a cellular flame acquires a finger-like shape, exhibiting strong acceleration, which lasts for a short time, until a flame skirts contacts a passage wall. In particular, in a 2D geometry, no detonation is predicted for methane combustion, while in the case of propane, the detonation may occur for near-stoichiometric, slightly fuel-rich burning, with equivalence ratios in the range $1 \leq \phi \leq 1.2$. For the cylindrical geometry, this range varies as $0.9 \leq \phi \leq 1.2$ and $0.8 \leq \phi \leq 1.3$ for methane and propane, respectively.

The entire acceleration scenario may promote the total burning rate by up to two orders of magnitude, to near-sonic flame velocities. Obviously, such fast flame spreading constitutes a substantial disaster, especially in enclosures and limited spacing such as in coalmines. Moreover, in addition to the direct disaster of such a fast flame, it may facilitate the deflagration-to-detonation transition, thereby leading to additional hazards for both personnel and equipment such as spreading of strong shock waves.

Acknowledgments

The co-authors recognise Vitaly Bychkov, who passed away when the work was in progress.

Disclosure statement

No potential conflict of interest was reported by the authors.

Funding

This study is sponsored by the US National Science Foundation (NSF) [through the CAREER Award #1554254] (V.A.), prior to which it was supported by the Alpha Foundation for the Improvement of Mine Safety and Health, Inc. (ALPHA FOUNDATION) [through the Award #AFSTI14-05] (V.A.) as well as West Virginia University's Program to Stimulate Competitive Research (PSCoR) and West Virginia University's Senate Award for Research and Scholarship. The views, opinions and recommendations expressed herein are solely those of the authors and do not imply any endorsement by the ALPHA FOUNDATION, its directors and staff.

References

- [1] K. Chatrathi, J.E. Going, and B. Grandestaff, *Flame propagation in industrial scale piping*, *Process Saf. Prog.* 20 (4) (2001), pp. 286–294.
- [2] M. Silvestrini, B. Genova, G. Parisi, and F.L. Trujillo, *Flame acceleration and DDT run-up distance for smooth and obstacles filled tubes*, *J. Loss Prev. Process Ind.* 21 (2008), pp. 555–562.
- [3] X. Chen, Y. Zhang, and Y. Zhang, *Effect of CH₄-air ratios on gas explosion flame microstructure and propagation behaviors*, *Energies* 5 (2012), pp. 4132–4146.
- [4] M. Bi, C. Dong, and Y. Zhou, *Numerical simulation of premixed methane-air deflagration in large L/D closed pipes*, *Appl. Therm. Eng.* 40 (2012), pp. 337–342.
- [5] L. Kjalldman, *Numerical flow simulation of dust deflagration*, *Power Technol.* 71 (1992), pp. 163–169.

- [6] Q. Liu, C. Bai, X. Li, L. Jiang, and W. Dai, *Coal dust/air explosions in a large-scale tube*, Fuel 89 (2010), pp. 329–335.
- [7] T. Skjold, D. Castellanos, K. Olsen, and R. Eckhoff, *Experimental and numerical investigation of constant volume dust and gas explosions in a 3,6-m flame acceleration tube*, J. Loss Prev. Process Ind. 30 (2014), pp. 164–176.
- [8] R.W. Houim and E.S. Oran, *Structure and flame speed speed of dilute and dense layered coal-dust explosions*, J. Loss Prev. Process Ind. 36 (2015), pp. 214–222.
- [9] B. Gardner, R. Winter, and M. Moore, *Explosion development and deflagration to detonation in coal dust/air suspensions*, Proc. Combust. Inst. 21 (1986), pp. 335–343.
- [10] W. Bartknecht, *Bundesinstitut für Arbeitsschutz (Bifa)*, Koblenz, Germany, 1971.
- [11] W. Bartknecht, *Staubexplosionen*, Springer, Verlag, 1987.
- [12] A.K. Oppenheim, A.J. Laderman, and P.A. Urtiew, *The onset of retonation*, Combust. Flame 6 (1962), pp. 193–197.
- [13] P.A. Urtiew and A.K. Oppenheim, *Experimental observations of the transition to detonation in an explosive gas*, Proc R. Soc. Lond. Ser. A. Math. Phys. 295 (1940) (1966), pp. 13–28.
- [14] C. Clanet and G. Searby, *On the “tulip flame” phenomenon*, Combust. Flame 105 (1996), pp. 225–238.
- [15] V. Bychkov, V. Akkerman, G. Fru, A. Petchenko, and L.E. Eriksson, *Flame acceleration in the early stages of burning in tubes*, Combust. Flame 150 (2007), pp. 263–276.
- [16] H. Xiao, R.W. Houim, and E.S. Oran, *Formation and evolution of distorted tulip flames*, Combust. Flame 162 (11) (2015), pp. 4084–4101.
- [17] V. Bychkov and M. Liberman, *Dynamics and stability of premixed flames*, Phys. Rep. 325 (2000), pp. 115–237.
- [18] D. Bradley, T.M. Cresswell, and J.S. Puttock, *Flame acceleration due to flame-induced instabilities in large-scale explosions*, Combust. Flame 124 (4) (2001), pp. 551–559.
- [19] T. Becker and F. Ebert, *Vergleich zwischen experiment und theorie der explosion grober, freier gaswolken*, Chem. Ing. Tech. 57 (1) (1985), pp. 42–45.
- [20] D. Valiev, V. Akkerman, M. Kuznetsov, L.E. Eriksson, C.K. Law, and V. Bychkov, *Influence of gas compression on flame acceleration in the early stage of burning in tubes*, Combust. Flame 160 (2013), pp. 97–111.
- [21] V. Bychkov, A. Petchenko, V. Akkerman, and L.E. Eriksson, *Theory and modelling of accelerating flames in tubes*, Phys. Rev. E. 72 (2005), p. 046307.
- [22] D. Valiev, V. Bychkov, V. Akkerman, and A. Petchenko, *Flame acceleration in channels with obstacles in the deflagration-to-detonation transition*, Combust. Flame 157 (2010), pp. 1012–1021.
- [23] V. Akkerman and V. Bychkov, *Turbulent flame and the Darrieus-Landau instability in a three-dimensional flow*, Combust. Theory Modelling 7 (2003), pp. 767–794.
- [24] M.A. Liberman, M.F. Ivanov, A.D. Kiverin, M.S. Kuznetsov, A.A. Chukalovsky, and T.V. Rakhimova, *Deflagration-to-detonation transition in highly reactive combustible mixtures*, Acta Astronaut. 67 (2010), pp. 688–701.
- [25] V. Akkerman, V. Bychkov, A. Petchenko, and L.E. Eriksson, *Accelerating flames in cylindrical tubes with non-slip at the walls*, Combust. Flame 145 (2006), pp. 206–219.
- [26] Z. Chen and Y. Ju, *Theoretical analysis of the evolution from ignition kernel to flame ball and planar flame*, Combust. Theory Modelling 11 (3) (2007), pp. 427–453.
- [27] M. Burke, Z. Chen, Y. Ju, and F. Dryer, *Effect of cylindrical confinement on the determination of laminar flame speeds using outwardly propagating flames*, Combust. Flame 156 (4) (2009), pp. 771–779.
- [28] C.K. Law, *Combustion Physics*, Cambridge University Press, New York, 2006.
- [29] Y.B. Zeldovich, G.I. Barenblatt, V.B. Librovich, and G.M. Makhviladze, *Mathematical Theory of Combustion and Explosion*, Consultants Bureau, New York, 1985.
- [30] V. Akkerman, C.K. Law, and V. Bychkov, *Self-similar accelerative propagation of expanding wrinkled flames and explosion triggering*, Phys. Rev. E. 83 (2011), p. 026305.
- [31] V. Bychkov and M. Liberman, *Stability and fractal structure of a spherical flame in a self-similar regime*, Phys. Rev. Lett. 76 (1996), pp. 2814–2817.
- [32] P. Pelce and P. Clavin, *Influence of hydrodynamics and diffusion upon the stability limits of laminar premixed flames*, J. Fluid Mech. 124 (1982), pp. 219–237.
- [33] S.G. Davis, J. Quinard, and G. Searby, *Markstein numbers in counterflow methane- and propane-air flames: A computational study*, Combust. Flame 7 (2003), pp. 767–794.

- [34] K. Seshadri, A.L. Berlad, and V. Tangirala, *The structure of premixed particle-cloud flames*, *Combust. Flame* 89 (1992), pp. 333–342.
- [35] S. Ranganathan, M. Lee, V. Akkerman, and A.S. Rangwala, *Suppression of premixed flames with inert particles*, *J. Loss Prev. Process Ind.* 35 (2015), pp. 46–51.
- [36] C. Morley, *Gaseq*, (2005), [Online]. Available at <http://www.c.morley.dsl.pipex.com/>.
- [37] Y. Xie, V. Raghavan, and A.S. Rangwala, *Study of interaction of entrained coal dust particles in lean methane-air premixed flames*, *Combust. Flame* 159 (2012), pp. 2449–2456.
- [38] R.W. Houim and E.S. Oran, *Numerical simulation of dilute and dense layered coal-dust explosions*, *Proc. Combust. Inst.* 35 (2015), pp. 2083–2090.
- [39] S. Demir, H. Sezer, and V. Akkerman, *Effect of local variations of the laminar flame speed on the global finger-flame acceleration scenario*, *Combust. Sci. Technol.* submitted.